The 2020 M_w 6.8 Elazığ (Turkey) earthquake reveals rupture behavior of the East Anatolian Fault

Léa Pousse-Beltran[1], Edwin Nissen[1], Eric A. Bergman[2], Musavver Didem Cambaz[3], Élyse Gaudreau[1], Ezgi Karasözen[4], and Fengzhou Tan[1]

[1]School of Earth and Ocean Sciences, University of Victoria, Victoria BC, Canada
[2]Global Seismological Services, Golden CO, USA
[3]Kandilli Observatory and Earthquake Research Institute, Boğaziçi University, İstanbul, Turkey
[4]Alaska Earthquake Center, University of Alaska Fairbanks, Fairbanks AK, USA

Key Points:

- The mainshock propagated mostly westwards from a nucleation point on an abrupt ∼10° fault bend
- Only one rupture termination corresponds to an established EAF segment boundary, and the rupture may partially overlap with an 1874 earthquake
- The mainshock exhibits a pronounced shallow slip deficit, that is not fully recovered through early shallow afterslip

Keywords : earthquake, Turkey, geodesy, seismology

Corresponding author: Léa Pousse-Beltran, `leapousse@uvic.ca`

Abstract

The 2020 M_w 6.8 Elazığ earthquake was the largest along the Eastern Anatolian Fault (EAF) in over a century and so provides valuable insights into its rupture behavior. Because the EAF is of low-to-intermediate structural maturity, this earthquake could also help refine relations between cumulative fault offset and characteristics including rupture velocity, shallow slip deficit, and afterslip. We use satellite geodesy and seismology to detail the mainshock rupture, postseismic deformation and aftershocks. The mainshock propagated mostly westwards at $\sim$2 km/s from a nucleation point on an abrupt $\sim$10° fault bend. Only one end of the rupture corresponds to an established EAF segment boundary, the earthquake may have propagated into the slip zone of the 1874 M $\sim$7.1 Gölcuk Gölu earthquake. It exhibits a pronounced ($\sim$80%) shallow slip deficit, only a small proportion of which is recovered by early aseismic afterslip.

Plain Language Summary

[We investigate the 2020 M_w 6.8 Elazığ (Turkey) earthquake, the largest along the Eastern Anatolian Fault in over a century. Anatolian faults are emblematic within the earthquake science community, but most attention has focused on the North Anatolian fault which ruptured repeatedly during the 20th Century, and relatively little is known about the East Anatolian Fault. We use satellite geodesy and seismology to map fault motions during the earthquake, after the earthquake, and in its aftershock sequence. Documenting relations between this earthquake, previous earthquakes, and early postseismic deformation is pivotal to gain a better understanding in what drives rupture behavior. Our results show that previous structural models of the EAF were only partially successful in predicting the end points of the 2020 rupture, and that many aspects of this earthquake are characteristic of structurally immature faults. These results are important for seismic hazard assessment in this region.]

1 Introduction

The $\sim$500 km-long, left-lateral East Anatolian Fault (EAF) in southeastern Turkey forms the active plate boundary between Arabia and Anatolia (Figure 1a, b). The $\sim$WSW-trending EAF encompasses several releasing and restraining bends and stepovers (Arpat & Şaroğlu, 1972; Bozkurt, 2001), segmentation that may be influenced by its obliquity to E–W structures of the SE Anatolia Thrust Zone, part of the Bitlis-Zagros suture (Şengör

& Yilmaz, 1981; Yılmaz, 1993). Together with the conjugate, right-lateral North Anatolian Fault (NAF), the EAF accommodates westward extrusion of Anatolia from the Arabia-Eurasia collision zone at a slip-rate of ∼11 mm/yr (Cetin et al., 2003; Walters et al., 2014; Aktug et al., 2016). Both faults are associated with numerous destructive historical earthquakes (Ambraseys & Jackson, 1998), but whereas the NAF hosted twelve $M_w \geq 6.7$ ruptures during the past century (e.g., A. Barka, 1996; Tibi et al., 2001), the EAF has a notable scarcity of large instrumental events. This hampers our understanding of its kinematics, structural characteristics and rupture behavior.

The January 24 2020 M_w 6.8 Elazığ earthquake struck at 17:55 UTC (20:55 local time), causing damage across the southern Elazığ and Malatya provinces, killing ∼41 people and injuring ∼1,600 others (Çetin et al., 2020). It was the largest EAF earthquake in more than a century, motivating a detailed examination of its rupture characteristics. Nucleating close to Lake Hazar — a contested EAF segment boundary (Figure 1c) — it could help resolve uncertainties in local fault structure and its controls on rupture propagation (A. A. Barka & Kadinsky-Cade, 1988; Aksoy et al., 2007; Garcia Moreno et al., 2011; Duman & Emre, 2013). Furthermore, its relations to large historical ruptures in 1874 and 1875 (to the NE) and 1893 and 1905 (to the SW) (Ambraseys (1989); Figure 1c) could provide an informative test of the characteristic earthquake and seismic gap models (McCann et al., 1979; Schwartz & Coppersmith, 1984; Kagan et al., 2012). Documenting the surface expression of the Elazığ earthquake also provides important context to paleoseismic studies of the EAF (Cetin et al., 2003; Garcia Moreno et al., 2011; Hubert-Ferrari et al., 2020). Finally, the central EAF has cumulative geomorphological or geological offsets of ∼9–26 km (Duman & Emre, 2013), making it of low-to-intermediate structural maturity according to the definition of Dolan and Haravitch (2014). The Elazığ earthquake could therefore help refine relations between fault structural maturity and characteristics such as rupture velocity, off-fault deformation, shallow slip deficits, and afterslip (e.g., Dolan & Haravitch, 2014; Socquet et al., 2019; Li et al., 2020).

The main goal of this paper is to characterize the Elazığ mainshock faulting, its early aftershock activity and postseismic deformation. We use Interferometric Synthetic Aperture Radar (InSAR) and optical satellite imagery, teleseismic back-projections, regional moment tensors and calibrated hypocentral relocations. We go on to discuss relations between the 2020 earthquake and proposed EAF segment boundaries, historical ruptures, and background seismicity. Finally, we assess our results in the context of emerging conceptual models for fault rupture behaviour and consider implications for future earthquake potential along the EAF.

2 Methods

2.1 Satellite geodesy

We investigated coseismic deformation using European Space Agency (ESA) Sentinel-1 interferograms collected on January 21–22 and 27–28 2020 on ascending tracks 43A and 116A and descending tracks 21D and 123D (Supplementary Table S1). Interferograms were processed in GAMMA and unwrapped using the branch-cut algorithm; unwrapping errors were then manually fixed. We estimated the mainshock fault geometry and slip distribution using a well-established elastic dislocation modeling approach (e.g., Wright et al., 1999; Elliott et al., 2012) based upon Okada's (1985) formulae. The unwrapped interferograms were first downsampled using a Quadtree algorithm (Jónsson et al., 2002). We then used Powell's minimization algorithm (Press et al., 1992) to solve for the minimum misfit strike, dip, rake, slip, latitude, longitude, length and top and bottom depths of a rectangular fault plane embedded within an elastic half-space (Supplementary Text S1), as well as E–W and N–S orbital ramps and the zero displacement level. Local minima are avoided by repeating the inversion hundreds of times with randomly-sampled starting parameters and retaining only the lowest residual solution (Clarke et al., 1997; Wright et al., 1999). Ascending and descending data were weighted equally in the inversion, but track 21D was weighted one third relative to 123D since it only spans that fraction of the rupture. We found that two model faults were needed to match the observed displacements well, but that fixing these faults to the observed EAF surface trace produced worse misfits than free location solutions (Supplementary Text S1, Figures S1–S4, and Table S2). We then extended and subdivided these model fault planes into 3 $\times$ 3 km subfaults and solved for the slip distribution. We applied a Laplacian smoothing operator and assessed misfits using the L-curve criterion in order to determine the appropriate degree of smoothing (Wright et al., 2003).

To investigate early postseismic deformation, we processed four consecutive, 6 day interferograms on each of the four available tracks, starting with the earliest postseismic scenes on January 27–28 2020 (Figure S5). These revealed afterslip localized along the fault trace, but the relatively low signal-to-noise ratio precluded us applying the same inversion procedure as for coseismic slip. To quantify afterslip, we first estimated east and vertical displacement components from tracks 43A and 123D, InSAR being largely insensitive to north–south motion (Wright et al., 2004). Observing no clear vertical displacement gradient localized along the fault (Figure S6a), we assume that the east component reflects fault-parallel, not fault-normal, displacement. We projected the east component onto the 244°-oriented fault and then constructed ∼8 km-long fault-perpendicular profiles at intervals along strike. On each profile, we modelled displacement (y) at perpendicular distance (x) with an arctan function to solve for uniform slip U and locking depth D (Savage & Burford, 1973). Adding a linear term ($R \times x$) to account for residual orbital ramps, we obtained a function model $y = \frac{U}{\pi} \times \arctan(\frac{x}{D}) + Rx$, that we fitted using the least squares Levenberg-Marquardt algorithm (Moré, 1978).

We also investigated horizontal surface deformation using an optical image correlation (OIC) of pre- and post-earthquake 10 m-resolution ESA Sentinel-2 images and the Cosi-CORR software (Leprince et al., 2007). OIC can detect near-fault surface deformation caused by shallow slip in regions where radar interferograms often decorrelate, and can thus help refine InSAR slip models (Xu et al., 2016). Unfortunately, the epicentral region was obscured by dense cloud cover after the earthquake with the earliest usable post-seismic image collected on February 27 2020; our results therefore capture both coseismic and five weeks of postseismic deformation. The pre-event image was acquired on November 9 2019. Processing details are provided in Supplementary Text S2.

2.2 Seismology

We imaged the mainshock rupture propagation using a phase-weighted relative back projection of high-frequency P waves recorded across a teleseismic station array (Ishii et al., 2005; F. Tan et al., 2019). After trials with data from a number of regions, we chose an Alaskan array of 119 stations at distances of 69–86° and with high cross-correlation coefficients for the first few seconds of the P wave. Theoretical travel times were calculated from a grid of nodes across the source region to each station (Supplementary Text S3) and waveforms were cleaned with a 0.3–2 Hz band-pass filter. Assuming a source depth of 6 km — consistent with our InSAR modeling results — we mapped relative energy at 1 s intervals and a 10 s sliding window for the duration of the rupture.

We estimated source mechanisms of early aftershocks (up to February 17 2020) by modeling regional waveforms recorded at distances of 50–380 km by stations of the Kandilli Observatory and Earthquake Research Institute (KOERI; Boğaziçi University Kandilli Observatory and Earthquake Research Institute (2001)) and Disaster and Emergency Management Authority of Turkey (AFAD) seismic networks (Figure 1b). Thirty events were studied, of which half yielded robust, stable solutions. Between 6 and 20 stations were used for each event, yielding azimuthal gaps of at most 140 °. Seismograms were filtered between 0.02–0.09 Hz, with the exact frequency band for each event selected after analyzing signal-to-noise ratios and station epicentral distances. Green's functions were estimated for the local velocity model (Supplementary Text S3) using the discrete wavenumber method (Bouchon, 1981). We solved for the best point source moment tensor by minimizing misfits between observed and synthetic waveforms using an iterative deconvolution inversion (Kikuchi & Kanamori, 1991) implemented in the ISOLA software package (E. N. Sokos & Zahradník, 2008). The fifteen robust solutions (listed in Supplementary Table S3) each meet the variance reduction and other quality criteria defined by Zahradník and Sokos (2018); one is shown as an example in Supplementary Figure S8.

Finally, we used local, regional and teleseismic phase arrivals to relocate hypocenters of the mainshock, 30 early aftershocks (up to February 20 2020), and ∼300 well-recorded background events starting in 1971. Data were gathered from regional networks operated by KOERI, AFAD, and the European-Mediterranean Seismological Centre (EMSC), and from the International Seismological Centre (ISC) bulletin. Target earthquakes were separated into five clusters: the first focused on the 2020 sequence and nearby seismicity in 2019; a second targeted earlier events along the Pürtürge EAF segment; and a third, fourth and fifth covered segments to the ENE and WSW (Supplementary Figure S9a). Each cluster was relocated using the *mloc* program (Bergman & Solomon, 1990; Walker et al., 2011), which separates the relocation into two distinct inverse problems reliant on customized phase arrival time data (Jordan & Sverdrup, 1981). Firstly, arrival times of all phases at all distances were used to determine cluster vectors that relate individual locations and origin times to the hypocentroid (the geometrical mean for all events), with 90% confidence usually in the range ∼1–2 km. Secondly, direct Pg and Sg phases at epicentral distances of $<1°$ (Figure 1b) were used to establish the absolute location and origin time of the hypocentroid, with uncertainties of <1 km. Combining these steps yields 'calibrated' hypocenters and uncertainties, listed in Table S4. Bespoke crustal velocity models were determined for each cluster by analyzing fits to Pg and Pn at the closest stations and Pn and Sn at regional distances (Supplementary Text S3 and Figure S9b).

3 Results

3.1 Background seismicity and foreshock activity

Of the background events relocated to the Pürtürge segment of the EAF, eight are sufficiently large (M_w 4.9–5.7) as to be ascribed teleseismic focal mechanisms (Figures 1b–c, Figure 2a). Four of these have predominantly strike-slip mechanisms and form a linear trend ~5 km north of the main fault surface trace. Since this distance exceeds relocation uncertainties, we suggest either that the Pürtürge segment dips northwards, with these events nucleating near the base of the fault, or that a previously-unrecognized northern EAF strand crosses this area. We also observe one moderate and several smaller earthquakes south of the town of Sivrice, consistent with a minor, southern splay fault observed by Bulut et al. (2012). The largest of these has a normal faulting mechanism, perhaps related to development of Lake Hazar basin (Aksoy et al., 2007; Garcia Moreno et al., 2011; Duman & Emre, 2013).

The most recent of the focal mechanism events — on April 4 2019 (M_w 5.3) and December 27 2019 (M_w 4.9) — are each located within ~5 km of the 2020 Elazığ mainshock epicenter, and so we classify them as foreshocks (Figure 2a,c). Calibrated focal depths along the Pürtürge segment range from 4–18 km with a peak at 10–13 km (inset to Figure 2c), in close agreement with previous regional studies (O. Tan et al., 2011; Bulut et al., 2012) and consistent with a central EAF locking depth of ~15 km inferred from satellite geodesy (Walters et al., 2014; Aktug et al., 2016).

3.2 Mainshock coseismic faulting

Coseismic interferograms exhibit larger northern and smaller southern fringe lobes that close near Sivrice in the ENE and near Pürtürge in the WSW (Figure 3a). Inverting the unwrapped interferograms, we obtained two co-linear model faults with strike 244° (Figure 2b, c). The ~36 km-long eastern model fault dips 80° N and is left-lateral (rake 3°), while the ~15 km-long western fault dips 64° N and has a small normal component (rake −18°). These northward dips are required to match the distinct asymmetry to the fringe pattern and are consistent with the range of published seismological mechanisms (Table 1).

At the surface, our model faulting resembles the mapped trace of the EAF (Duman & Emre, 2013), except that the observed $\sim 10°$ fault bend is manifest in our model as a small left stepover. Attempts at fixing the model fault surface projection to the observed, kinked surface trace resulted in worse misfits, and so we consider our geometry to be the best approximation of fault structure at the scale of the seismogenic zone. Nevertheless, the model fault geometry in the region of intersection may reflect limitations to the modeling approach as opposed to a real segment boundary; instead, the faulting may 'twist' gradually from steeper dips in the east to gentler ones in the west. Maximum slip of 2.4 m occurs close to the model fault intersection at 6–9 km depth and only <0.5 m slip reaches the shallowest patches (Figure 3c). Though the resolution of the shallowest slip is limited by InSAR decorrelation along the surface trace, these results are consistent with the absence of primary surface rupturing observed in preliminary field investigations (Çetin et al., 2020) and suggest a pronounced shallow slip deficit.

The InSAR model moment of 1.79×10^{19} Nm (M_w 6.8) closely matches the Global Centroid Moment Tensor (GCMT) seismic moment of 1.77×10^{19} Nm, implying that most the slip inferred from InSAR occurred coseismically. Our relocated hypocenter lies midway along the eastern model fault segment at a depth of ~ 8 km (Figure 2c). $\sim 80\%$ of the InSAR model moment occurs WSW of the epicenter, and only $\sim 20\%$ ENE of it. Back projection results show that high frequency energy is also released almost exclusively WSW of the epicenter, consistent with a rupture velocity in that direction of ~ 2 km/s and a rupture duration of ~ 20 s (Figure 2b). A single peak in back-projected energy a few kilometers ENE of the epicenter matches a local peak in InSAR model slip and confirms that the rupture is not entirely unilateral. However, the smaller (<0.5 m) coseismic slip resolved by InSAR at the far ENE end of the rupture is below the resolution of the back projection method (F. Tan et al., 2019).

3.3 Postseismic displacements

We observe a sharp phase jump localized on the EAF in the earliest postseismic 6 day interferogram (January 27/28 to February 2/3). Although later interferograms suffer from decorrelation, this phase jump seems to have disappeared by the time of the last pair processed (February 14/15 to 20/21). We used the cumulative 24 day interferograms (January 28–February 21) to estimate early postseismic afterslip, focusing WSW of the mainshock epicenter where coseismic slip was greatest and where InSAR near-field displacements are most coherent (Figure 4a). Fitting fault-perpendicular profiles with the arctan model, we estimate maximum afterslip of ∼15 cm, less than 7% of the peak coseismic slip (Figure 4b). The greatest afterslip occurs close to the mainshock epicenter and appears to be buried, with minimum misfit locking depths of ∼1 km. WSW of the epicenter, afterslip decreases rapidly to ∼2–3 cm and the locking depth diminishes to near zero, indicating postseismic surface rupturing.

Horizontal coseismic and postseismic displacements mapped with OIC are dominated by topographic artefacts without a clear coseismic signal, although a long-wavelength signal near the fault in the E-W displacement field may reflect left-lateral slip (Figure 4c). Displacement measurement uncertainties are ∼0.75 m in the East-West component and ∼1.0 m in the North-South component (Supplementary Text S2). The lack of a distinct coseismic signal at this resolution is consistent with the pronounced shallow slip deficit inferred from our coseismic and postseismic InSAR models.

3.4 Aftershock seismicity

Most aftershocks exhibit left-lateral mechanisms along or parallel to the EAF (Figure 2c). We observe notable clusters close to the mainshock hypocenter and at either end of the coseismic faulting (near Lake Hazar and Pürtürge). In contrast, very few aftershocks are associated with peak coseismic slip near the InSAR model fault intersection (Figures 2c and 3b). Many of the aftershocks — particularly within the concentrations at either end of the mainshock rupture — lie up to ∼10 km off the main trace of the EAF, suggesting activation of secondary faults within a damage zone (Liu et al., 2003). The easternmost aftershock studied here has a distinctive normal component, consistent with interpretations of the Lake Hazar basin as a releasing bend or pull-apart (Aksoy et al., 2007; Garcia Moreno et al., 2011; Duman & Emre, 2013).

Aftershock relocated focal depths range from 7–17 km whereas centroid depths from waveform modeling are 2–13 km (inset to Figure 2c). Use of an alternative velocity model (Acarel et al., 2019) increased waveform model centroid depths by on average ∼2 km, reducing but not eliminating this discrepancy. These results mimic relations observed in comparably-instrumented regions elsewhere (Karasözen et al., 2016, 2018; Gaudreau et al., 2019) and likely reflect the depth resolution limitations of both methods, together with the propensity for earthquakes to nucleate deeper within the seismogenic zone and rupture upwards.

4 Discussion

4.1 Relations with previous seismicity and with structural segmentation of the EAF

The Elazığ mainshock nucleated in a zone of apparent structural complexity between the villages of Uslu and Doğanyol, where Duman and Emre (2013) mapped a pair of small (<500 m) right steps and an abrupt bend in the EAF surface trace (Figure 2c). The eastern right step (at Uslu) is manifest as a ∼1 km fault gap and the western right step (north of the Karakaya reservoir) as a ∼4 km stretch of parallel, overlapping fault strands. Just west of these parallel strands, the EAF abruptly changes strike by ∼10°. The April 4 and December 27 2019 foreshocks provide further evidence of structural complexity in this area (Figure 2a). The April 4 M_w 5.3 foreshock likely ruptured the EAF close to the eastern fault step at Uslu. The December 27 M_w 4.9 foreshock was located at the fault bend north of Doğanyol; both its nodal planes are at high angles to the EAF, suggesting rupture of a subsidiary structure or splay.

The 2020 mainshock nucleated within this zone of complexity, between the two foreshocks (Figure 2b, c). Towards the ENE, the mainshock terminated at Lake Hazar, interpreted by Cetin et al. (2003) and Duman and Emre (2013) as a left-stepping releasing bend, by Aksoy et al. (2007) as a horst structure, and by Garcia Moreno et al. (2011) as a continuous, unsegmented fault section. Towards the WNW, it propagated past the ∼10° fault bend — manifest in our simplified slip model as a releasing step — to terminate on a relatively straight section of the fault west of Pürtürge. Here, our model fault geometry is slightly oblique to the mapped surface trace, hinting that at the scale of the seismogenic zone the fault has a somewhat skewed, non-planar geometry (Diederichs et al., 2019).

Large historical earthquakes in 1874, 1875, 1893 and 1905 are each attributed to the central EAF on the basis of damage patterns and — in the earliest of these events — reports of surface rupturing (Ambraseys, 1989). The May 3 1874 (M ∼7.1) and March

27 1875 (M ∼6.7) Gölcuk Gölu earthquakes were both centered upon Lake Hazar, whose former name they bear (Figure 1c). The 1874 earthquake devastated settlements along a ∼50 km corridor extending from Uslu, ∼15 km west of the lake, to Tenik, ∼20 km east of it. Surface rupturing is suspected from reports that the south side of the lake was uplifted by ∼1–2 m and that the valley NE of the lake was "rent" (Ambraseys, 1989; Ambraseys & Jackson, 1998). The reported damage distribution hints that faulting may have extended west of the lake, too, but this cannot be confirmed. It is therefore unclear whether the 2020 earthquake ruptured into the slip area of the 1874 earthquake, or stopped short of it. The 1875 earthquake was assigned the same macroseismic epicenter as the 1874 event, but its rupture extents are poorly constrained. The March 2 1893 (M ∼7.1) and December 4 1905 (M_s 6.8) Malatya earthquakes were both centered on the Yarpuzlu restraining bend, with damage focused upon settlements between Erkenek (in the west) and Pütürge (in the east) (Ambraseys, 1989). The eastern limit to the zone of maximum damage in both earthquakes therefore approximates the western limit of faulting in the 2020 earthquake. However, without more precise information on the fault extents of the 1893 and 1905 earthquakes, it is unclear whether they are separated from, connected to, or partially overlap with the 2020 rupture area.

Duman and Emre (2013) used the apparent spatial separation between the 1875 and 1893 ruptures to argue for a seismic gap along the Pütürge segment of the EAF. However, our relocation of background seismicity marks this as amongst the most seismically active EAF segments in the past few decades, not normally the hallmark of a supposed seismic gap. During the period 1964–2019, the Pütürge segment hosted eight earthquakes large enough ($M_w > \sim 5$) to be ascribed teleseismic focal mechanisms, more than any other EAF segment (Figure 1b). Similarly, Bulut et al. (2012) observed that between 2007 and 2011 — and discounting the aftershock zone of the 2010 M_w 6.1 Kovancılar earthquake — the densest activity of small-to-moderate events ($M_w > \sim 3$) along the whole EAF occurred between Pütürge and Lake Hazar: the eventual 2020 rupture zone.

4.2 Earthquake behaviour and structural maturity

Our coseismic InSAR modeling suggests that only ∼20% of the peak slip at depth reaches the surficial model fault patches, implying a shallow slip deficit of ∼80% (Figure 3c). Other studies have shown that apparent shallow slip deficits can arise from a lack of resolution in near field InSAR data or from model uncertainties at shallow depth

(Xu et al., 2016; Huang et al., 2017). However, in our case, the absence of a clear surface rupturing signal in optical imagery or from the preliminary field reconnaissance by Çetin et al. (2020) implies that the deficit inferred from InSAR modeling is real.

Dolan and Haravitch (2014) compared shallow slip deficits of six M_w >7.1 strike-slip earthquakes, and observed that those on immature faults — defined as having cumulative offsets of <25 km — had smaller ratios of surface slip to deep slip (∼50–60%) than those on mature faults (∼85–95%). This is thought to reflect the progressive localization of slip as fault zones evolve over many earthquake cycles, with more of the shallow strain manifest as inelastic, distributed deformation along immature faults (e.g., Kaneko & Fialko, 2011; Zinke et al., 2015; Roten et al., 2017). Earthquakes somewhat smaller than the cut-off of M_w 7.1 considered by Dolan and Haravitch (2014) might have even more pronounced shallow slip deficits because of the scaling of moment magnitude with slip area. For example, the 2003 Bam and 2017 Jiuzhaigou earthquakes, both M_w 6.5, each had pronounced shallow slip deficits, exhibited minimal postseismic afterslip, and ruptured structurally-immature faults (Fialko et al., 2005; Li et al., 2020). The central EAF is well-established as of low-to-intermediate structural maturity, with total offsets of ∼9–26 km (Duman & Emre, 2013), providing a plausible explanation for the low (∼20%) ratio of surface slip to peak slip at depth. The small amounts (<15 cm) of observed shallow afterslip, slow (∼2 km/s) rupture speed, and scattered aftershocks are also consistent with relatively immature faults (e.g., Liu et al., 2003; Perrin et al., 2016; Li et al., 2020). This strongly motivates studies that seek to characterize and quantify off-fault deformation along the EAF, and future morphotectonic or paleoseismological investigations should be undertaken with the awareness that a large proportion of deformation may be distributed away from the main fault trace.

Ultimately, the shallow slip deficit must eventually be recovered for long-term slip to be conserved; we now consider how and when that might occur. Early, localized, shallow afterslip is limited to <7% of the maximum coseismic slip magnitude, accounting only for a small portion of the deficit (Figure 4). More could be recovered by persistent shallow creep during the interseismic period, especially since serpentinite-rich ophiolitic rocks mapped near the Pürtürge segment could plausibly exhibit velocity-strengthening frictional behavior (Khalifa et al., 2018; Karaoğlan et al., 2013; Yılmaz, 1993). However, afterslip decays rapidly and disappears completely by mid February (Figure S5), inconsistent with persistent creep (e.g., Çakir et al., 2012). Ultimately, longer geodetic timeseries are probably required in order to determine whether aseismic processes might account for the shallow slip deficit, or whether the shallow part of the fault is locked (e.g., Fielding et al., 2009).

This raises the possibility that the shortfall in shallow slip could be recovered by future earthquakes. For example, a deficit in surface slip observed in the 1981 M_w 7.1 Sirch earthquake on the Gowk fault in Iran was later accounted for by the shallower 1998 M_w 6.6 Fandoqa event (Berberian et al., 2001). To address whether 2020 rupture released all the accumulated strain along the Pürtürge segment of the EAF and the expectation of a larger or shallower event re-rupturing this section to fill the shallow slip deficit, we consider it in the context of the characteristic earthquake model (Schwartz & Coppersmith, 1984). If the 2020 rupture were characteristic, then average coseismic slip of ∼1 m coupled with strain accumulation rates of ∼11 mm/yr (Walters et al., 2014; Aktug et al., 2016) would imply an average repeat interval of just ∼90 years. While this approximates the time since large earthquakes in 1874, 1893 and 1905, these historical events were centered on adjacent segments of the EAF and likely did not rupture the entire Pürtürge segment (Ambraseys, 1989; Ambraseys & Jackson, 1998). Moreover, a ∼3,800 year record of turbidites in Lake Hazar are interpreted to indicate a ∼190 year average recurrence interval that captures large events on both the Pürtürge and Palu segments of the EAF (Hubert-Ferrari et al., 2020). This implies either that the 2020 M_w 6.8 earthquake was not characteristic and that larger ruptures are possible. Future seismic hazard assessments of the EAF should take into account this possibility.

5 Conclusions

The January 24 2020 M_w6.8 Elazığ ruptured the Pürtürge segment of the EAF from a nucleation point near an abrupt, ∼10° bend in the fault surface trace. It was preceded by two nearby (∼5 km distance) moderate foreshocks on April 4 and December 27 2019. ENE of the epicenter, the mainshock may have propagated into the rupture zone of the 1874 M ∼7.1 Gölcuk Gölu earthquake, and it halted in the Lake Hazar basin, previously identified as a major EAF segment boundary. Towards the WSW, it propagated at ∼2 km/s and terminated after ∼20 s along a straight, structurally-simple section of the Pürtürge fault segment; relations with the 1893 M ∼7.1 and 1905 M_s 6.9 Malatya earthquakes are unclear. Overall, our results indicate that previous structural segmentation models of the central EAF are oversimplified and that this was not a characteristic earthquake.

The mainshock rupture exhibits a pronounced shallow slip deficit, which is only partially recovered through shallow afterslip. These characteristics — as well as the slow rupture propagation speed and abundant off-fault background and aftershock seismicity — probably reflect the low-to-moderate structural maturity of the central EAF. The possibility for significant off-fault deformation should be taken into account in future paleoseismological and morphotectonic studies of the EAF.

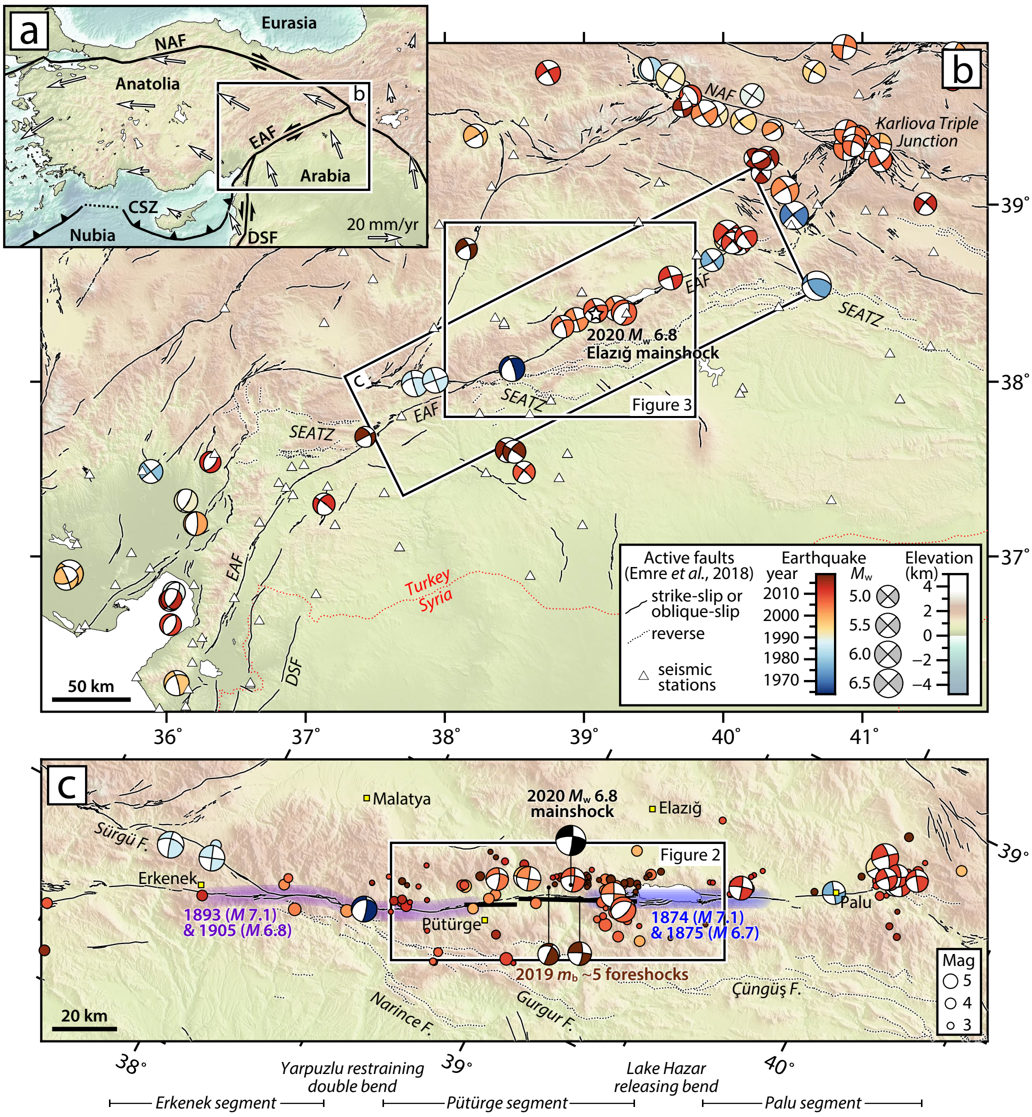

Figure 1. (Caption next page.)

Figure 1. (Previous page.) (a) Tectonic setting with plate boundaries (black lines) and representative GPS velocities relative to stable Eurasia (white arrows, from Kreemer et al. (2014)). CSZ = Cyprus Subduction Zone, DSF = Dead Sea Fault, EAF = East Anatolian Fault, NAF = North Anatolian Fault. (b) Focal mechanisms, station distribution, and active faults in SE Anatolia (SEATZ = Southeast Anatolia Thrust Zone). Teleseismic focal mechanisms, colored by year up to 2019, are from McKenzie (1972), Taymaz et al. (1991) and the U.S. Geological Survey (USGS) and Global Centroid Moment Tensor (GCMT) catalogs. We use our own, relocated epicenters along the EAF and ISC-EHB epicenters elsewhere (Weston et al., 2018). Triangles are seismic stations used for direct calibration of our relocation clusters and for regional waveform modeling. (c) Close-up of the central EAF. Colored shading shows zones of maximum damage associated with historical earthquakes in 1874 and 1875 (blue) and 1893 and 1905 (purple), from Ambraseys (1989). Focal mechanisms are as in (b) with the addition of two 2019 foreshocks and the 2020 Elazığ mainshock. Circles show earthquakes without focal mechanisms, colored the same but scaled differently. Thick black lines are surface projections of our preferred InSAR model faults for the 2020 mainshock. Below the map, we show the central EAF segmentation scheme of Duman and Emre (2013).

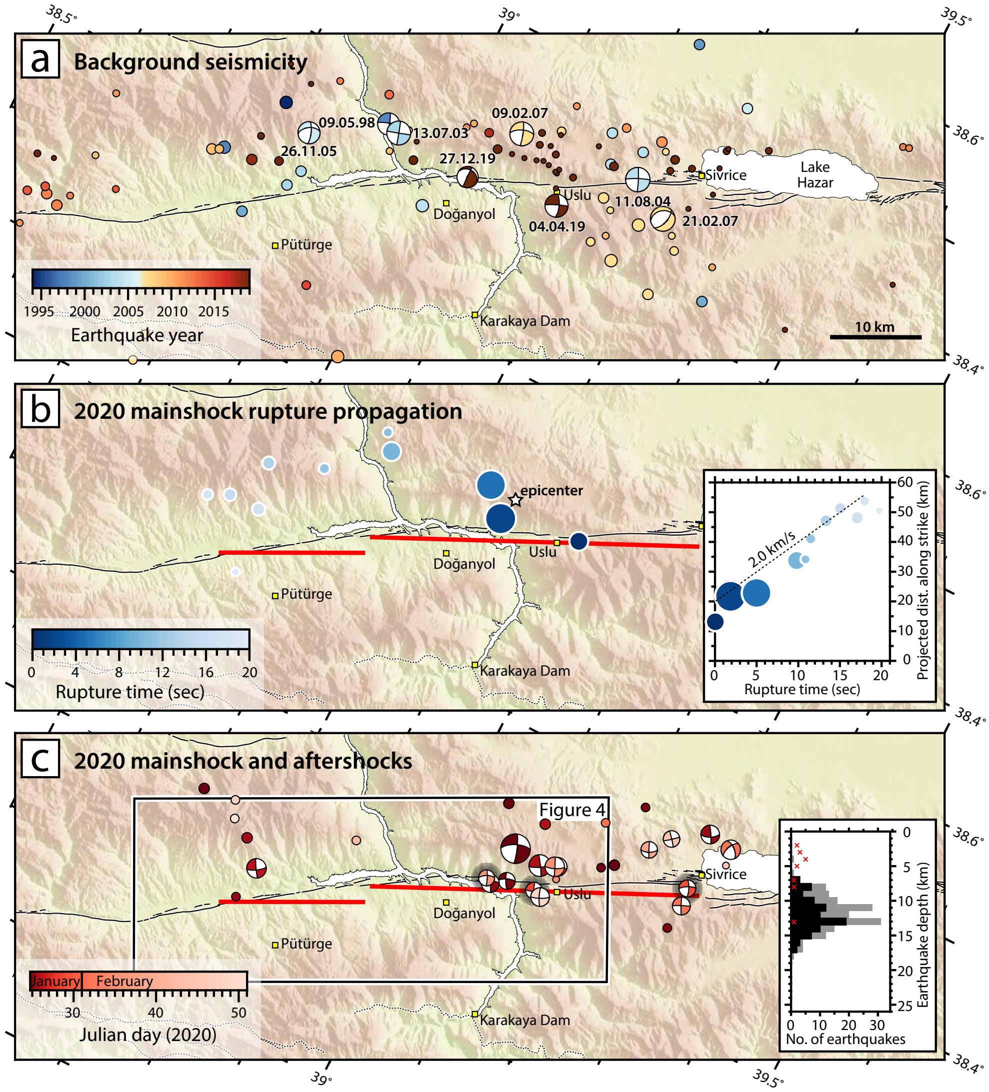

Figure 2. (Caption next page.)

Figure 2. (Previous page.) (a) Background seismicity (1994–2019) along the central and eastern Pürtürge segment of the EAF, plotted at relocated epicenters, colored by year, and scaled by magnitude as in Figure 1c. Focal mechanisms are from the GCMT and KOERI catalogs. Faults are as in Figure 1b–c. (b) Back projection results, scaled by relative energy and colored by rupture time. Thick red lines are surface projections of our preferred InSAR model faults for the 2020 Elazığ mainshock. Inset shows sub-event distance along strike versus rupture time, with distances projected onto a line of strike 244° and 0 km marking the eastern end of the InSAR model fault. (c) Elazığ mainshock and aftershock seismicity, colored by date and plotted at our relocated epicenters where possible (shadowed mechanisms are plotted at EMSC locations). The mainshock mechanism is from the GCMT catalog; aftershocks are best double couple solutions our own regional waveform modeling. Inset shows relocated focal depths of our local clusters, with 2019–2020 events in black and older events in gray. Red crosses show aftershock centroid depths from regional waveform modeling.

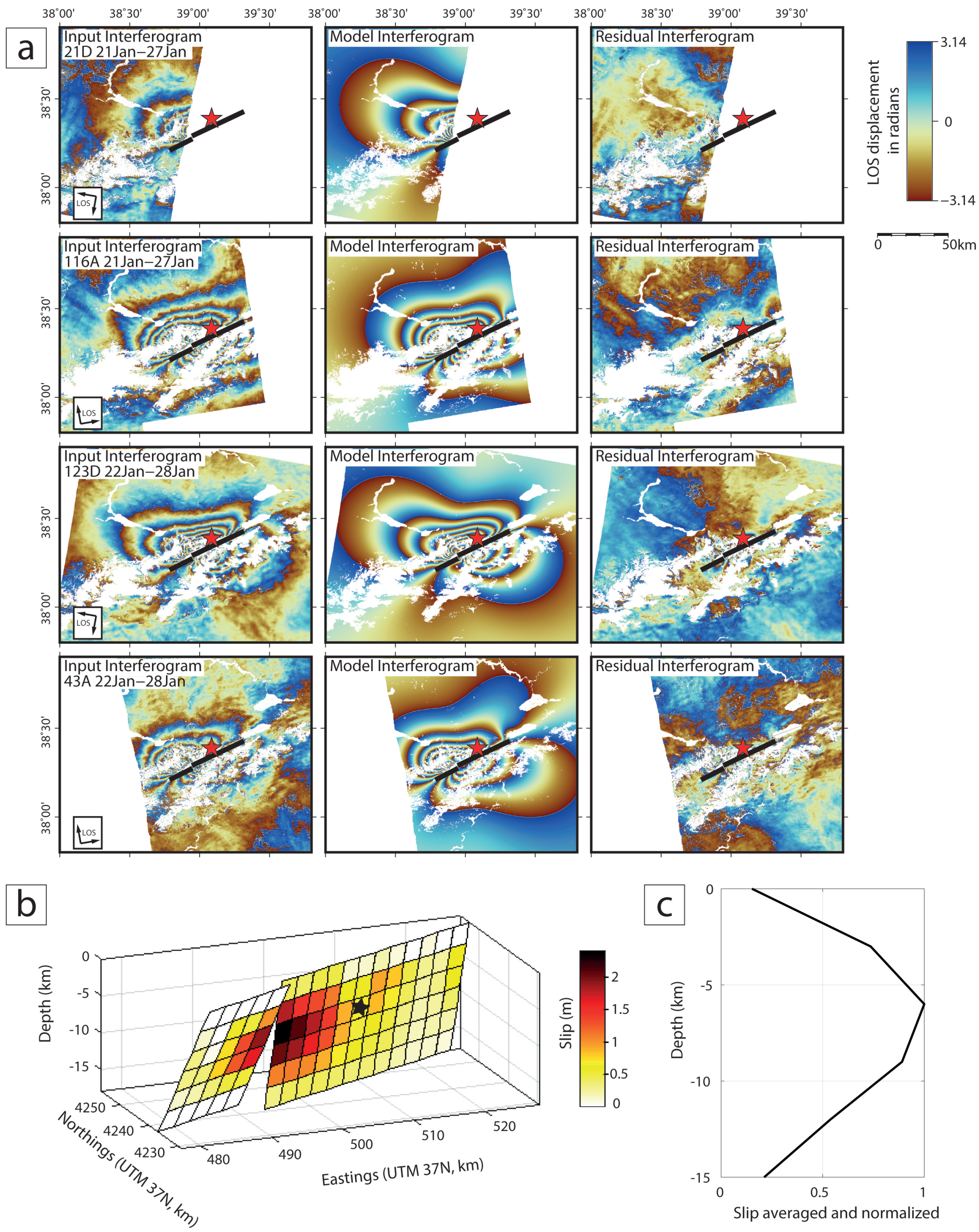

Figure 3. (a) From top to bottom: interferograms on track 21D, 116A, 123D and 43A. From left to right: observed, model and residual interferograms. Modeling was performed using unwrapped interferograms but the results are shown re-wrapped in order to accentuate deformation gradients and facilitate comparisons with data. The thick black line is the surface projection of the model faults and the red star is the relocated epicenter. (b) Model slip distribution. Each fault patch measures 3 × 3 km. The black star shows the relocated hypocenter at 8 km depth, projected on the fault plane. (c) Distribution of normalized average slip versus depth.

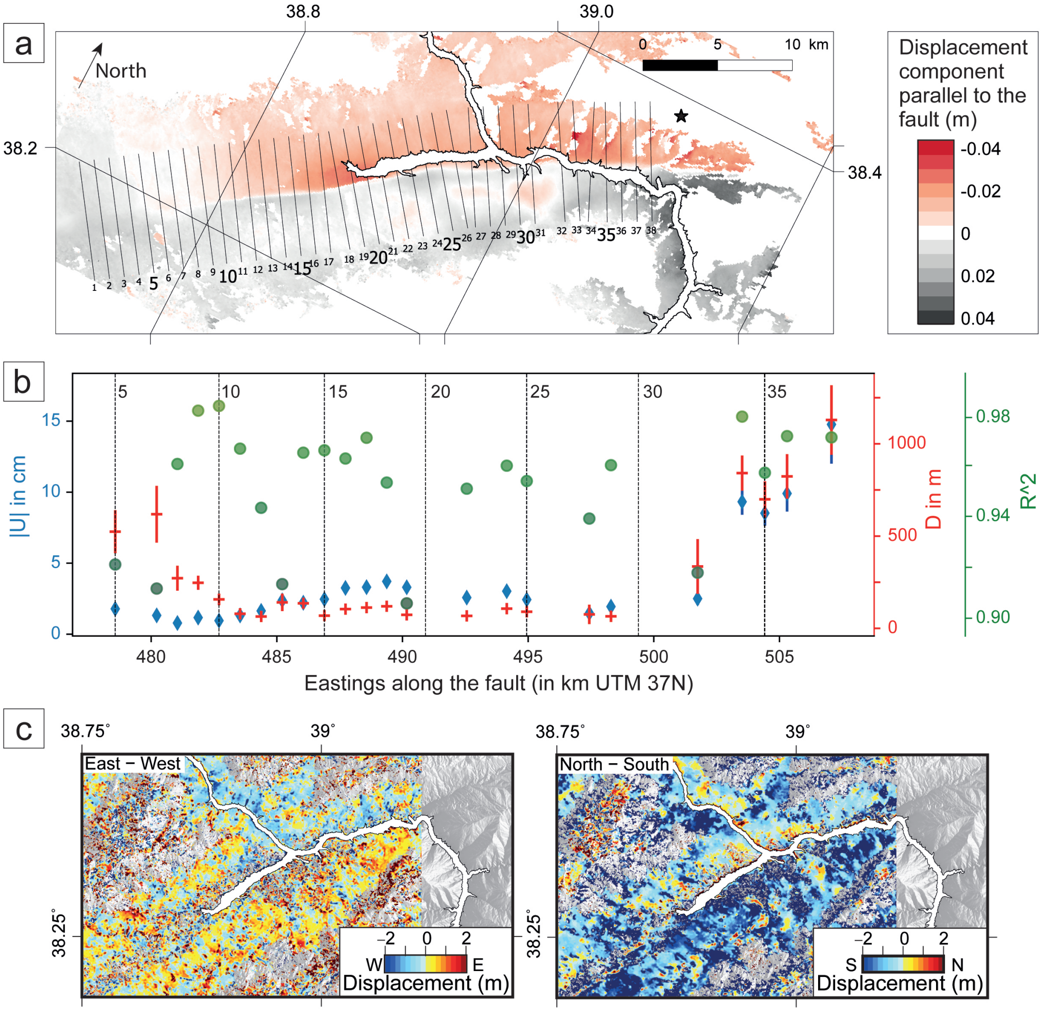

Figure 4. (a) Horizontal displacements projected onto the fault-parallel direction (244°) during the early postseismic period (January 27–February 21 2020), estimated from tracks 43A and 123D. The black star is the relocated epicenter. Profile lines 1 to 38 were used to fit our afterslip model. We only used profiles with more than 75% of data available. Observed and modeled profiles are plotted in Figure S6b. (b) Afterslip modeling results. Blue diamonds are slip U, red crosses are locking depth D, and green dots show coefficients of determination R^2 (only results with $R^2 > 0.9$ are shown). Vertical dashed lines labelled with numbers (5, 10, etc.) refer to profile numbers displayed in (a). (c) Horizontal (left) E–W and (right) N–S coseismic-to-early postseismic displacements mapped from optical image correlation (OIC) of Sentinel-2 images acquired on November 9 2019 and February 27 2020.

Table 1. Source parameters of the 2020 Elazığ mainshock. GCMT = Global Centroid Moment Tensor project; USGS = United States Geological Survey Comprehensive Earthquake Catalog; Mww = W-phase moment tensor; Mwr = regional moment tensor; Mwb = body wave tensor; AFAD = Disaster and Emergency Management Authority of Turkey; KOERI = Kandilli Observatory and Earthquake Research Institute. Lon. and lat. refer to the longitude and latitude of the InSAR model fault center surface projections, the GCMT centroid, and the USGS epicenter. Depth refers to the peak slip depth of the InSAR model and the centroid depth of the GCMT, USGS and KOERI solutions; AFAD list both the centroid and focal depths.

Source	Lon.	Lat.	Strike	Dip	Rake	Depth	Seismic moment	M_w
This study								
Eastern model fault	39.0648°	38.3363°	245°	80°	3°	6-9 km	1.36×10^{19} Nm	6.7
Western model fault	38.9349°	38.2655°	243°	64°	−18°	6-9 km	0.44×10^{19} Nm	6.4
Other mechanisms								
GCMT	39.00°	38.30°	246°	67°	−9°	12 km	1.77×10^{19} Nm	6.8
USGS Mww	39.088°	38.390°	245°	80°	−12°	22 km	1.39×10^{19} Nm	6.7
USGS Mwr	39.088°	38.390°	246°	77°	0°	11 km	0.60×10^{19} Nm	6.5
USGS Mwb	39.088°	38.390°	250°	85°	1°	16 km	1.23×10^{19} Nm	6.7
AFAD	39.0630°	38.3593°	248°	76°	1°	8/15 km	–	6.8
KOERI	39.29°	38.52°	248°	87°	−4°	10 km	1.29×10^{19} Nm	6.7

Acknowledgments

The University of Victoria Earthquakes group are supported by the Natural Sciences and Engineering Research Council of Canada, the Canada Foundation for Innovation, the BC Knowledge Development Fund, a Canada Research Chair to E. N., and an NSERC Alexander Graham Bell Canada Graduate Scholarship to E. G. All data used in this study are freely available through the links listed below. We used Copernicus Sentinel-1 InSAR and Sentinel-2 optical imagery (`https://scihub.copernicus.eu/`). Teleseismic waveform data were obtained from IRIS Data Services, and specifically the IRIS Data Management Center (`https://ds.iris.edu/ds/nodes/dmc/`), which are funded through the Seismological Facilities for the Advancement of Geoscience and EarthScope (SAGE) Proposal of the National Science Foundation (EAR-1261681). Regional waveforms were obtained from KOERI `http://eida-service.koeri.boun.edu.tr`). Arrival time data were obtained from the ISC Bulletin (`https://doi.org/10.31905/D808B830`). Our relocation clusters have been added to the Global Catalog of Calibrated Earthquake Locations (`https://www.sciencebase.gov/catalog/item/59fb91fde4b0531197b16ac7`), where additional station maps and travel time residual plots are available. We used supplementary location parameters from the relocated ISC-EHB dataset (`https://doi.org/10.31905/PY08W6S3`), and focal mechanisms from the GCMT project (`https://www.globalcmt.org/`), the USGS Comprehensive Earthquake Catalog (`https://earthquake.usgs.gov/data/comcat/`), AFAD (`https://deprem.afad.gov.tr/?lang=en`) and KOERI. Figures were plotted with *Generic Mapping Tools* software (Wessel et al., 2013).

References

Acarel, D., Cambaz, M. D., Turhan, F., Mutlu, A. K., & Polat, R. (2019). Seismotectonics of Malatya Fault, Eastern Turkey. *Open Geosciences*, *11*(1).

Aksoy, E., Inceoez, M., & Köçyiğit, A. (2007). Lake Hazar basin: A negative flower structure on the east anatolian fault system (EAFS), SE Turkey. *Turk. J. Earth Sci.*, *16*(3), 319–338.

Aktug, B., Ozener, H., Dogru, A., Sabuncu, A., Turgut, B., Halicioglu, K., … Havazli, E. (2016). Slip rates and seismic potential on the East Anatolian Fault System using an improved GPS velocity field. *J. Geodynamics*, *94*, 1–12.

Ambraseys, N. N. (1989). Temporary seismic quiescence: SE Turkey. *Geophys. J. Int.*, *96*(2), 311–331.

Ambraseys, N. N., & Jackson, J. A. (1998). Faulting associated with historical and recent earthquakes in the Eastern Mediterranean region. *Geophys. J. Int.*, *133*, 390–406.

Arpat, E., & Şaroğlu, F. (1972). Some observations and thoughts on the East Anatolian fault. *Bull. Miner. Res. Explor. Inst. Turkey*, *73*, 44–50.

Ayoub, F., Leprince, S., & Avouac, J.-P. (2017). User's guide to COSI-CORR co-registration of optically sensed images and correlation [Computer software manual].

Barka, A. (1996). Slip distribution along the North Anatolian fault associated with the large earthquakes of the period 1939 to 1967. *Bull. Seismol. Soc. Am.*, *86*(5), 1238–1254.

Barka, A. A., & Kadinsky-Cade, K. (1988). Strike-slip fault geometry in Turkey and its influence on earthquake activity. *Tectonics*, *7*(3), 663–684.

Berberian, M., Jackson, J. A., Fielding, E., Parsons, B. E., Priestley, K., Qorashi, M., … Baker, C. (2001, August). The 1998 March 14 Fandoqa earthquake (M_w 6.6) in Kerman province, southeast Iran: re-rupture of the 1981 Sirch earthquake fault, triggering of slip on adjacent thrusts and the active tectonics of the Gowk fault zone. *Geophys. J. Int.*, *146*, 371–398.

Bergman, E. A., & Solomon, S. C. (1990). Earthquake swarms on the Mid-Atlantic Ridge — Products of magmatism or extensional tectonics? *J. Geophys. Res.*, *95*, 4943–4965.

Bouchon, M. (1981). A simple method to calculate Green's functions for elastic layered media. *Bull. Seismol. Soc. Am.*, *71*(4), 959–971.

Boğaziçi University Kandilli Observatory and Earthquake Research Institute. (2001). *International Federation of Digital Seismograph Networks. Dataset/Seismic Network.* doi: 10.7914/SN/KO

Bozkurt, E. (2001). Neotectonics of Turkey — a synthesis. *Geodinamica Acta*, *14*(1), 3–30.

Bulut, F., Bohnhoff, M., Eken, T., Janssen, C., Kılıç, T., & Dresen, G. (2012). The East Anatolian Fault Zone: Seismotectonic setting and spatiotemporal characteristics of seismicity based on precise earthquake locations. *J. Geophys. Res.*, *117*.

Çakir, Z., Ergintav, S., Özener, H., Dogan, U., Akoglu, A. M., Meghraoui, M., &

Reilinger, R. (2012). Onset of aseismic creep on major strike-slip faults. *Geology*, *40*(12), 1115–1118.

Cetin, H., Güneyli, H., & Mayer, L. (2003). Paleoseismology of the Palu-Lake Hazar segment of the East Anatolian Fault Zone, Turkey. *Tectonophys.*, *374*(3), 163–197.

Çetin, K. Ö., Ilgac, M., Can, G., Çakır, E., & Söylemez, B. (2020). *January 24, 2020 Elazığ-Sivrice earthquake (M_w=6.8) Reconnaissance Study Report* (Tech. Rep. No. METU/EERC 2020-01). Middle East Technical University. doi: 10.17603/ds2-9jz1-e287

Clarke, P. J., Paradissis, D., Briole, P., England, P. C., Parsons, B. E., Billiris, H., ... Ruegg, J.-C. (1997). Geodetic investigation of the 13 May 1995 Kozani-Grevena (Greece) earthquake. *Geophys. Res. Lett.*, *24*, 707–710.

Şengör, A. M. C., & Yilmaz, Y. (1981). Tethyan evolution of Turkey: A plate tectonic approach. *Tectonophys.*, *75*(3), 181–241.

Diederichs, A., Nissen, E. K., Lajoie, L. J., Langridge, R. M., Malireddi, S. R., Clark, K. J., ... Tagliasacchi, A. (2019). Unusual kinematics of the Papatea fault (2016 Kaikōura earthquake) suggest anelastic rupture. *Sci. Adv.*, *5*(10).

Dolan, J. F., & Haravitch, B. D. (2014). How well do surface slip measurements track slip at depth in large strike-slip earthquakes? The importance of fault structural maturity in controlling on-fault slip versus off-fault surface deformation. *Earth Planet. Sci. Lett.*, *388*, 38–47.

Duman, T. Y., & Emre, O. (2013). The East Anatolian Fault: geometry, segmentation and jog characteristics. In A. H. F. Robertson, O. Parlak, & U. C. Ünlügenç (Eds.), *Geological Development of Anatolia and the Easternmost Mediterranean Region* (Vol. 372, pp. 495–529). Geol. Soc. London Spec. Publ..

Elliott, J. R., Nissen, E. K., England, P. C., Jackson, J. A., Lamb, S., Li, Z., ... Parsons, B. (2012). Slip in the 2010-2011 Canterbury earthquakes, New Zealand. *J. Geophys. Res.*, *117*.

Fialko, Y., Sandwell, D., Simons, M., & Rosen, P. (2005). Three-dimensional deformation caused by the Bam, Iran, earthquake and the origin of shallow slip deficit. *Nature*, *435*, 295–299.

Fielding, E. J., Lundgren, P. R., Bürgmann, R., & Funning, G. J. (2009). Shallow fault-zone dilatancy recovery after the 2003 Bam earthquake in Iran. *Nature*, *458*(7234), 64–68.

Garcia Moreno, D., Hubert-Ferrari, A., Moernaut, J., Fraser, J. G., Boes, X., Van Daele, M., ... De Batist, M. (2011). Structure and recent evolution of the Hazar Basin: a strike-slip basin on the East Anatolian Fault, Eastern Turkey. *Basin. Res.*, *23*(2), 191–207.

Gaudreau, É., Nissen, E. K., Bergman, E. A., Benz, H. M., Tan, F., & Karasözen, E. (2019). The August 2018 Kaktovik earthquakes: Active tectonics in northeastern Alaska revealed with InSAR and seismology. *Geophys. Res. Lett.*, *46*, 14412–14420.

Huang, M. H., Fielding, E. J., Dickinson, H., Sun, J., Gonzalez-Ortega, J. A., Freed, A. M., & Bürgmann, R. (2017). Fault geometry inversion and slip distribution of the 2010 Mw 7.2 El Mayor-Cucapah earthquake from geodetic data. *J. Geophys. Res.*, *122*(1), 607–621.

Hubert-Ferrari, A., Lamair, L., Hage, S., Schmidt, S., Namık Çağatay, M., & Avşar, U. (2020, May). A 3800 yr paleoseismic record (Lake Hazar sediments, eastern Turkey): Implications for the East Anatolian Fault seismic cycle. *Earth Planet. Sci. Lett.*, *538*.

Ishii, M., Shearer, P. M., Houston, H., & Vidale, J. E. (2005). Extent, duration and speed of the 2004 Sumatra-Andaman earthquake imaged by the Hi-Net array. *Nature*, *435*, 933–936.

Jónsson, S., Zebker, H., Segall, P., & Amelung, F. (2002). Fault Slip Distribution of the 1999 M_w 7.1 Hector Mine, California, Earthquake, Estimated from Satellite Radar and GPS Measurements. *Bull. Seismol. Soc. Am.*, *92*, 1377–1389.

Jordan, T. H., & Sverdrup, K. A. (1981). Teleseismic location techniques and their application to earthquake clusters in the South-Central Pacific. *Bull. Seismol. Soc. Am.*, *71*, 1105–1130.

Kagan, Y. Y., Jackson, D. D., & Geller, R. J. (2012). Characteristic earthquake model, 1884–2011, RIP. *Seismol. Res. Lett.*, *83*(6), 951–953.

Kaneko, Y., & Fialko, Y. (2011). Shallow slip deficit due to large strike-slip earthquakes in dynamic rupture simulations with elasto-plastic off-fault response. *Geophys. J. Int.*, *186*(3), 1389–1403.

Karaoğlan, F., Parlak, O., Klötzli, U., Koller, F., & Rızaoğlu, T. (2013). Age and duration of intra-oceanic arc volcanism built on a suprasubduction zone type oceanic crust in southern Neotethys, SE Anatolia. *Geosci. Frontiers*, *4*(4), 399–408.

Karasözen, E., Nissen, E., Bergman, E. A., Johnson, K. L., & Walters, R. J. (2016). Normal faulting in the Simav graben of western Turkey reassessed with calibrated earthquake relocations. *J. Geophys. Res.*, *121*, 4553–4574.

Karasözen, E., Nissen, E., Büyükakpınar, P., Cambaz, M. D., Kahraman, M., Ertan, E. K., ... Özacar, A. A. (2018). The 2017 July 20 M_w 6.6 Bodrum–Kos earthquake illuminates active faulting in the Gulf of Gökova, SW Turkey. *Geophys. J. Int.*, *214*(1), 185–199.

Kennett, B. L. N., & Engdahl, E. R. (1991, May). Traveltimes for Global Earthquake Location and Phase Identification. *Geophys. J. Int.*, *105*, 429–465.

Kennett, B. L. N., Engdahl, E. R., & Buland, R. (1995, July). Constraints on seismic velocities in the Earth from traveltimes. *Geophys. J. Int.*, *122*, 108–124.

Khalifa, A., Çakir, Z., Owen, L. A., & Kaya, Ş. (2018). Morphotectonic analysis of the East Anatolian Fault, Turkey. *Turk. J. Earth Sci.*, *27*, 110–126.

Kikuchi, M., & Kanamori, H. (1991). Inversion of complex body waves—iii. *Bull. Seismol. Soc. Am.*, *81*(6), 2335–2350.

Kreemer, C., Blewitt, G., & Klein, E. C. (2014). A geodetic plate motion and Global Strain Rate Model. *gcubed*, *15*(10), 3849–3889.

Leprince, S., Barbot, S., Ayoub, F., & Avouac, J.-P. (2007). Automatic and Precise Orthorectification, Coregistration, and Subpixel Correlation of Satellite Images, Application to Ground Deformation Measurements. *IEEE Trans. Geosci. Rem. Sens.*, *45*, 1529–1558. doi: 10.1109/TGRS.2006.888937

Li, Y., Bürgmann, R., & Zhao, B. (2020). Evidence of Fault Immaturity from Shallow Slip Deficit and Lack of Postseismic Deformation of the 2017 Mw 6.5 Jiuzhaigou Earthquake. *Bull. Seismol. Soc. Am.*, *110*(1), 154–165.

Liu, J., Sieh, K., & Hauksson, E. (2003). A Structural Interpretation of the Aftershock "Cloud" of the 1992 M_w 7.3 Landers Earthquake. *Bull. Seismol. Soc. Am.*, *93*(3), 1333–1344.

McCann, W. R., Nishenko, S. P., Sykes, L. R., & Krause, J. (1979). Seismic gaps and plate tectonics: seismic potential for major boundaries. In *Earthquake prediction and seismicity patterns* (pp. 1082–1147). Springer.

McKenzie, D. (1972). Active Tectonics of the Mediterranean Region. *Geophys. J. Int.*, *30*, 109–185.

Moré, J. J. (1978). The Levenberg-Marquardt algorithm: Implementation and theory. In G. A. Watson (Ed.), *Numerical analysis* (pp. 105–116). Springer Berlin Heidelberg.

Okada, Y. (1985). Surface deformation due to shear and tensile faults in a half-space. *Bull. Seismol. Soc. Am.*, *75*, 1135–1154.

Perrin, C., Manighetti, I., Ampuero, J.-P., Cappa, F., & Gaudemer, Y. (2016). Location of largest earthquake slip and fast rupture controlled by along-strike change in fault structural maturity due to fault growth. *J. Geophys. Res.*, *121*, 3666–3685.

Press, W. H., Teukolsky, S. A., Vetterling, W. T., & Flannery, B. P. (1992). *Numerical recipes in c: The art of scientific computing.* Cambridge: Cambridge University Press.

Roten, D., Olsen, K., & Day, S. (2017). Off-fault deformations and shallow slip deficit from dynamic rupture simulations with fault zone plasticity. *Geophys. Res. Lett.*, *44*(15), 7733–7742.

Savage, J. C., & Burford, R. O. (1973). Geodetic determination of relative plate motion in central California. *J. Geophys. Res.*, *78*(5), 832–845. doi: 10.1029/JB078i005p00832

Schwartz, D. P., & Coppersmith, K. J. (1984, July). Fault behavior and characteristic earthquakes: Examples from the Wasatch and San Andreas Fault Zones. *J. Geophys. Res.*, *89*(B7), 5681–5698.

Socquet, A., Hollingsworth, J., Pathier, E., & Bouchon, M. (2019). Evidence of supershear during the 2018 magnitude 7.5 Palu earthquake from space geodesy. *Nat. Geosci.*, *12*(3), 192–199.

Sokos, E., & Zahradník, J. (2013). Evaluating Centroid-Moment-Tensor Uncertainty in the New Version of ISOLA Software. *Seismol. Res. Lett.*, *84*(4), 656–665.

Sokos, E. N., & Zahradník, J. (2008). ISOLA a Fortran code and a Matlab GUI to perform multiple-point source inversion of seismic data. *Computers & Geosciences*, *34*, 967–977.

Tan, F., Ge, Z., Kao, H., & Nissen, E. (2019). Validation of the 3-D phase-weighted relative back projection technique and its application to the 2016 M_w 7.8

Kaikōura earthquake. *Geophys. J. Int.*, *217*(1), 375–388.

Tan, O., Pabuçcu, Z., Tapırdamaz, M. C., İnan, S., Ergintav, S., Eyidoğan, H., … Kuluöztürk, F. (2011). Aftershock study and seismotectonic implications of the 8 March 2010 Kovancılar (Elazığ, Turkey) earthquake ($M_W = 6.1$). *Geophys. Res. Lett.*, *38*(11).

Taymaz, T., EyidoğaAn, H., & Jackson, J. (1991). Source parameters of large earthquakes in the East Anatolian Fault Zone (Turkey). *Geophys. J. Int.*, *106*(3), 537–550.

Tibi, R., Bock, G., Xia, Y., Baumbach, M., Grosser, H., Milkereit, C., … Zschau, J. (2001). Rupture processes of the 1999 August 17 Izmit and November 12 Düzce (Turkey) earthquakes. *Geophys. J. Int.*, *144*(2), F1–F7.

Walker, R. T., Bergman, E. A., Szeliga, W., & Fielding, E. J. (2011). Insights into the 1968-1997 Dasht-e-Bayaz and Zirkuh earthquake sequences, eastern Iran, from calibrated relocations, InSAR and high-resolution satellite imagery. *Geophys. J. Int.*, *187*, 1577–1603.

Walters, R. J., Parsons, B., & Wright, T. J. (2014). Constraining crustal velocity fields with InSAR for Eastern Turkey: Limits to the block-like behavior of Eastern Anatolia. *J. Geophys. Res.*, *119*(6), 5215–5234.

Wessel, P., Smith, W. H. F., Scharroo, R., Luis, J., & Wobbe, F. (2013). Generic Mapping Tools: Improved Version Released. *Eos Trans. AGU*, *94*, 409–410.

Weston, J., Engdahl, E. R., Harris, J., Di Giacomo, D., & Storchak, D. A. (2018). ISC-EHB: reconstruction of a robust earthquake data set. *Geophys. J. Int.*, *214*(1), 474–484.

Wright, T. J., Lu, Z., & Wicks, C. (2003). Source model for the M_w 6.7, 23 October 2002, Nenana Mountain Earthquake (Alaska) from InSAR. *Geophys. Res. Lett.*, *30*(18).

Wright, T. J., Parsons, B. E., Jackson, J. A., Haynes, M., Fielding, E. J., England, P. C., & Clarke, P. J. (1999). Source parameters of the 1 October 1995 Dinar (Turkey) earthquake from SAR interferometry and seismic bodywave modelling. *Earth Planet. Sci. Lett.*, *172*, 23–37.

Wright, T. J., Parsons, B. E., & Lu, Z. (2004). Toward mapping surface deformation in three dimensions using InSAR. *Geophys. Res. Lett.*, *31*.

Xu, X., Tong, X., Sandwell, D. T., Milliner, C. W. D., Dolan, J. F., Hollingsworth, J., ... Ayoub, F. (2016). Refining the shallow slip deficit. *Geophys. J. Int.*, *204*(3), 1867–1886.

Yılmaz, Y. (1993). New evidence and model on the evolution of the southeast Anatolian orogen. *Geol. Soc. Am. Bull.*, *105*(2), 251–271.

Zahradník, J., & Sokos, E. (2018). ISOLA Code for Multiple-Point Source Modeling—Review. In S. Damico (Ed.), *Moment tensor solutions.* Springer, Cham.

Zinke, R., Dolan, J. F., Van Dissen, R., Grenader, J. R., Rhodes, E. J., McGuire, C. P., ... Hatem, A. E. (2015). Evolution and progressive geomorphic manifestation of surface faulting: A comparison of the Wairau and Awatere faults, South Island, New Zealand. *Geology*, *43*(11), 1019–1022.